



Enhanced photocatalytic activity of hierarchical macro/mesoporous TiO₂–graphene composites for photodegradation of acetone in air

Wenguang Wang, Jiaguo Yu*, Qunjun Xiang, Bei Cheng

State Key Laboratory of Advanced Technology for Material Synthesis and processing, Wuhan University of Technology, Luosh Road 122#, Wuhan 430070, PR China

ARTICLE INFO

Article history:

Received 2 January 2012
Received in revised form 18 February 2012
Accepted 28 February 2012
Available online 8 March 2012

Keywords:

Hierarchical
Macro/mesoporous
Graphene
Titania
Photocatalytic activity

ABSTRACT

Graphene, a single layer of graphite, possesses a unique two-dimensional structure, high conductivity, superior electron mobility and extremely high specific surface area, and can be obtained on a large scale at low cost. Thus, it has been regarded as an excellent catalyst support. Recently, graphene-based semiconductor photocatalysts have attracted more attention due to their enhanced photocatalytic activity. In this work, hierarchical macro/mesoporous TiO₂–graphene composites with low loadings (0–0.2 wt.%) of graphene were first produced by a simple one-step hydrothermal method using tetrabutyl titanate as the titanium precursor. The prepared composite samples presented enhanced photocatalytic activity in photodegradation of acetone in air. Graphene content exhibited an obvious influence on photocatalytic activity and the optimal graphene addition content was determined. At the optimal graphene concentration (0.05 wt.%), the prepared composites showed the highest photocatalytic activity, exceeding that of pure TiO₂ and Degussa P-25 by a factor of 1.7 and 1.6, respectively. The enhanced photocatalytic activity is due to graphene as an excellent electron acceptor and transporter, thus reducing the recombination of charge carriers and enhancing the photocatalytic activity. The transient photocurrent response experiment further confirmed the transfer of photogenerated electrons from TiO₂ to graphene and the suggested mechanism.

© 2012 Elsevier B.V. All rights reserved.

1. Introduction

Heterogeneous photocatalytic oxidation (PCO) has been studied for several decades and shown to be an effective method for dealing with the environmental pollution problems, such as air cleanup, water disinfection, hazardous waste remediation, and water purification [1–10]. Among various semiconductor photocatalysts, titania has attracted much attention due to its fascinating properties such as biological and chemical inertness, strong oxidizing power, cost-effective, and long-term stability against photocorrosion and chemical corrosions [11–18]. However, the fast recombination rate of the photoinduced electron–hole pairs in TiO₂ reduces the efficiency of the photocatalytic reactions significantly, thus limiting its practical applications. Several strategies have been developed to enhance the photocatalytic efficiency of TiO₂ photocatalyst. Besides traditional doping [19,20], metal deposition [21], surface sensitization and coupling of composite semiconductors [4,22], the combination of carbon with TiO₂ was confirmed to be an effective way for separating electron–hole pairs [23,24]. Up to now, a variety of TiO₂–carbon composites had been fabricated, such as TiO₂/carbon

nanotube [23,25], TiO₂/C₆₀ [24,26], TiO₂/activated-carbon composites [27], and so on. The photocatalytic activity of these TiO₂/carbon composites was indeed improved to a certain extent.

Graphene, an attractive carbon material with unique properties, has gained tremendous attention since Novoselov et al. succeeded in extracting single-atom-thick crystallites (graphene) from bulk graphite in 2004 [28]. Graphene possesses a unique electronic property, ensures an excellent mobility of charge carriers (200 000 cm² V^{−1} s^{−1}), and exhibits an extremely high theoretical specific surface area (~2600 m² g^{−1}) [29]. Moreover, functional graphene can be prepared through low-cost solution-based processes, which offer significant opportunities for functionalized graphene-based composite materials [30]. It was reported that decorating semiconductor materials with functional graphene can enhance their electronic [31], optoelectronic [32], electrocatalytic [33], and photocatalytic properties [34–36].

In recent years, the combination of TiO₂ and graphene had been proved to be an effective pathway to improve the photocatalytic activity of TiO₂ due to the excellent adsorbability and conductivity of graphene [33,37–39]. For example, Li et al. obtained a chemically bonded P25-graphene nanocomposite photocatalyst with a significant enhancement in photodegradation of methylene blue [37]. They attributed the high performance of P25-graphene to the enhanced adsorbability of dyes and efficient charge separation and transportation. Xiang et al. fabricated highly

* Corresponding author.

E-mail address: jiaguoyu@yahoo.com.cn (J. Yu).

active graphene-modified TiO₂ nanosheets composite photocatalysts for H₂ production [38]. They for the first time demonstrated that inexpensive metal-free carbon material can be used as an effective co-catalyst for photocatalytic water splitting. Du et al. prepared hierarchical ordered macro-mesoporous TiO₂-graphene composite films with significant enhancement of photocatalytic activity for degrading the methyl blue [39]. However, the aforementioned studies mainly focused on the photocatalytic behavior of TiO₂-graphene composites for organic dyes or other liquid organic contaminants degradation. There is still scarce work on the usage of TiO₂-graphene composites for photodegradation of volatile organic compounds (VOCs). It is well-known that VOCs are triggering serious environmental problems such as stratospheric ozone depletion and tropospheric ozone increment. Among VOCs, acetone is one of the principle indoor air pollutants and long-term inhalation of acetone may cause serious health disorders. Therefore, the degradation of gas-phased acetone is of particularly important.

It was demonstrated that crystalline anatase TiO₂ powders with hierarchical macro/mesoporous structures, reasonable phase structures and composition, good crystallization, and high BET-specific surface areas were beneficial to enhance the photocatalytic activity [40–44]. Herein, hierarchical macro/mesoporous TiO₂ particles incorporated with graphene were prepared by hydrothermal treatment of graphene oxide (GO) and hydrolyzates of tetrabutyl titanate (Ti(OC₄H₉)₄, TBOT) in an ethanol–water mixed solvent. The photocatalytic activity of the as-prepared samples was examined towards the degradation of gas-phase acetone under UV light irradiation. A low graphene loading (0–0.1 wt.%) significantly enhanced the photoactivity of TiO₂ powders. At the optimal loading of 0.05 wt.% graphene, TiO₂-graphene composites showed the highest photocatalytic activity. To the best of our knowledge, this is the first time to report the enhanced photoactivity of hierarchical macro/mesoporous TiO₂-graphene composites to gas-phase acetone, and a mechanism for the enhanced photocatalytic oxidation activity by graphene modification is proposed.

2. Experimental

2.1. Sample preparation

Hierarchical macro/mesoporous TiO₂-graphene composites were prepared by hydrothermal treatment of graphene oxide (GO) and hydrolyzates of TBOT in an ethanol–water solvent. All chemicals used in this study were analytical grade and were used without further purification. Distilled water was used in all experiments. Graphene oxide nanosheets were purchased from Nanjing XFNANO Materials Technology Corporation Limited, Nanjing, People's Republic of China. In a typical preparation procedure, 2.4 mg of GO was dissolved in a mixed solution of distilled water (100 mL) and ethanol (20 mL) by ultrasonic treatment for 2 h, and then 20 mL of TBOT was added dropwise to the above mixed solution without stirring. The above mixture was then transferred to a 200 mL Teflon-lined autoclave. The autoclave was sealed and maintained at 180 °C for 12 h. After hydrothermal reaction, the resulting composite powders were collected, washed with distilled water followed by rinsing in ethanol, and then dried in an oven at 80 °C for 2 h. To investigate the effect of graphene content on the photocatalytic activity of TiO₂-graphene composite, the weight percentages of graphene to TiO₂ were varied from 0 to 0.2 (0, 0.05, 0.1 and 0.2 wt.%) (see Table 1) and the resulting samples were labeled as TG- x , where x = 0, 0.05, 0.1 and 0.2, respectively.

2.2. Characterization

The X-ray diffraction (XRD) measurements were carried out by an X-ray diffractometer (type HZG41B-PC), using Cu K α radiation at a scan rate (2θ) of 0.05° s⁻¹. The X-ray photoelectron spectroscopy (XPS) measurement was carried out in an ultrahigh vacuum VG ESCALAB 210 electron spectrometer equipped with a multi-channel detector. The samples were excited by Mg K α (1253.6 eV) radiation (operated at 200 W) of a twin anode in the constant analyzer energy mode with a pass energy of 30 eV. All the binding energies at 284.8 eV were referenced to the C 1s peak of the surface adventitious carbon. Raman spectra were recorded at room temperature using a micro-Raman spectrometer (Renishaw InVia) in the backscattering geometry with a 514.5 nm Ar⁺ laser as an excitation source. The Brunauer–Emmett–Teller (BET) specific surface areas (S_{BET}) of the powders were analyzed by nitrogen adsorption in a Micromeritics ASAP 2020 nitrogen adsorption apparatus (USA). All the as-prepared samples were degassed at 150 °C prior to nitrogen adsorption measurements. Scanning electron microscopy (SEM) was performed on an S-4800 Field Emission SEM (FESEM, Hitachi, Japan) at an accelerating voltage of 10 kV. Transmission electron microscopy (TEM) analyses were conducted on a JEM-2100F electron microscope (JEOL, Japan), using an accelerating voltage of 200 kV.

2.3. Evaluation of photocatalytic activity

The photocatalytic activity measurements of the as-prepared TiO₂-graphene powders and Degussa P-25 (P25) were evaluated towards oxidation decomposition of acetone in air at ambient temperature using a 15 L photocatalytic reactor. The photocatalysts were prepared by coating an aqueous suspension of TiO₂-graphene powders (60 mL) onto three culture dishes with diameters of 7.0 cm, which were dried in an oven at 80 °C for 2 h and then cooled to room temperature before use. The weight of the photocatalyst used for each experiment was 0.3 g. The dishes coated with TiO₂-graphene powder photocatalysts were placed in the reactor and a small amount of acetone (12 ± 1 μ L) was injected into the reactor. The acetone vapor was allowed to reach adsorption equilibrium with the catalyst in the reactor prior to an experiment. The initial concentration of acetone after reaching the adsorption equilibrium was about 300 ± 20 ppm, which remained constant until a 15 W, 365 nm UV lamp (Cole-Parmer Instrument) in the reactor was switched on. The UV lamp intensity striking on the coating measured with a UV radiometer (Model UV-A, made in the Photoelectric Instrument Factory of Beijing Normal University) was 2.5 mW/cm², and the initial temperature was 25 ± 1 °C. The analysis of acetone, carbon dioxide, and water vapor concentration in the reactor was conducted on line by a Photoacoustic IR multigas monitor (INNOVA Air Tech Instruments Model 1412). Each set of experiment was followed for 60 min. During the photocatalytic reaction, a near 3:1 ratio of carbon dioxide product to acetone destroyed was observed, and the acetone concentration decreased steadily with increasing UV illumination time. The photocatalytic activity of the TiO₂ samples can be quantitatively evaluated by comparing the apparent reaction rate constants. The photocatalytic oxidation of acetone is a pseudo-first-order reaction, and its kinetics may be expressed as: $\ln(C_0/C) = kt$, where k is the apparent reaction rate constant and C_0 and C are the initial concentration and instantaneous concentration of acetone, respectively.

2.4. Photoelectrochemical measurements

Photocurrents were measured using an electrochemical analyzer (CHI660C Instruments) in a standard three-electrode system using the as-prepared samples as the working electrodes with an

Table 1Effects of graphene content on the physical properties of the hierarchical macro/mesoporous TiO₂–graphene samples.

Sample	Graphene (wt.%)	Average crystallite size (nm)	S _{BET} (cm ² /g)	Pore volume (cm ³ /g)	Average pore size (nm)
TG-0	0	7.9	170.0	0.33	7.34
TG-0.05	0.05	7.9	164.4	0.34	8.60
TG-0.1	0.1	7.8	160.2	0.33	8.03
TG-0.2	0.2	7.6	153.5	0.33	8.53

active area of ca. 0.5 cm², a platinum wire as the counter electrode, and Ag/AgCl (saturating KCl) as the reference electrode. A 300 W Xe arc lamp served as a UV-light source. The integrated light intensity was measured to be 25 mW cm^{−1} using a UV radiometer (UV-A). 1 M Na₂SO₄ aqueous solution was used as the electrolyte. For the working electrodes, 0.2 g of TiO₂–graphene composite was ground with 0.06 g of polyethylene glycol (PEG, molecular weight 20000) and 1.0 mL of ethanol to make slurry. Afterwards, the slurry was coated onto a 2 cm × 1.2 cm F-doped SnO₂–coated glass (FTO glass) electrode by the doctor blade method. Upon drying in an oven, the electrodes were calcined at 400 °C for 30 min. All investigated electrodes have a similar film thickness (~15 μm).

3. Results and discussion

3.1. Phase structures

The phase structures of the as-prepared samples were characterized by XRD measurements. Fig. 1 depicts the XRD patterns of TiO₂–graphene composite photocatalysts (samples TG-0, TG-0.05, TG-0.1 and TG-0.2) synthesized by a hydrothermal method with different graphene loading. It can be seen from Fig. 1 that all diffraction peaks can be readily indexed to anatase TiO₂ (JCPDS no. 21-1272). No characteristic diffraction peaks for carbon species were observed in the TiO₂–graphene composites, which is due to the low amount and relatively low diffraction intensity of graphene. Nevertheless, the existence of graphene can be determined by the following Raman spectra and XPS analysis. Further observation indicates that the full width at half maximum (FWHM) of the anatase peaks for TiO₂–graphene composites are slightly broadened with increasing amount of graphene, implying a slight decrease in the anatase crystallite size (as shown in Table 1). The incorporation of graphene into TiO₂ particles did not have much effect on the crystallite size of anatase TiO₂, possibly due to their low concentration.

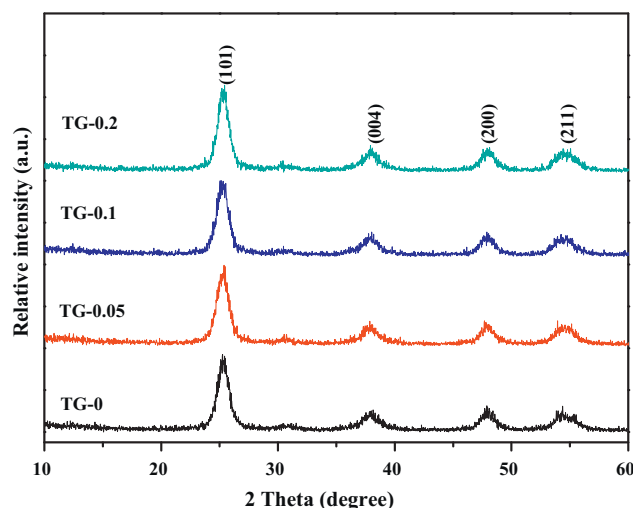


Fig. 1. XRD patterns of TiO₂–graphene composites (TG-0, TG-0.05, TG-0.1 and TG-0.2).

3.2. Raman spectra

Raman spectroscopy is a powerful nondestructive tool for distinguishing ordered and disordered crystal structures of carbon. The significant structural changes occurring during the hydrothermal reaction process from GO to graphene are also reflected in their Raman spectra. Fig. 2 shows a comparison of the Raman spectra of GO, pure TiO₂ (sample TG-0) and TiO₂–graphene composite (sample TG-0.05). In the case of GO, there are two typical Raman bands located at 1354 and 1596 cm^{−1}, which correspond to disordered sp² carbon (D-band) and well ordered graphite (G-band), respectively [36,38]. As for pure TiO₂ (sample TG-0), several characteristic bands at 146, 397, 516, and 637 cm^{−1} correspond to the E_g(1), B_{1g}(1), A_{1g} + B_{1g}(2) and E_g(2) modes of anatase, respectively [24,38]. For the TiO₂–graphene composite (TG-0.05), all the Raman bands for anatase can be observed. Further observation indicates that two characteristic peaks at about 1348 cm^{−1} (D band) and 1596 cm^{−1} (G band) for the graphitized structures are observed in the Raman spectrum of TG-0.05 (inset in Fig. 2), which correspond to the well-documented D and G bands, suggesting that the structure of graphene is maintained in the composite. Furthermore, an increased D/G intensity ratio is also observed in comparison with that of pure GO. This change suggests a decrease in the average size of the sp² domains upon reduction of the exfoliated GO, indicating that the GO has been well deoxygenated and reduced to graphene during the hydrothermal process [34,38]. In addition, it was reported that the treatment of GO with various alcohols under mild conditions afforded highly reduced products [45]. Hence, it is not surprising that GO was well reduced to graphene after the hydrothermal treatment.

3.3. XPS analysis

The chemical states of the graphene oxide and TiO₂–graphene composite were further studied by XPS. Fig. 3 shows the

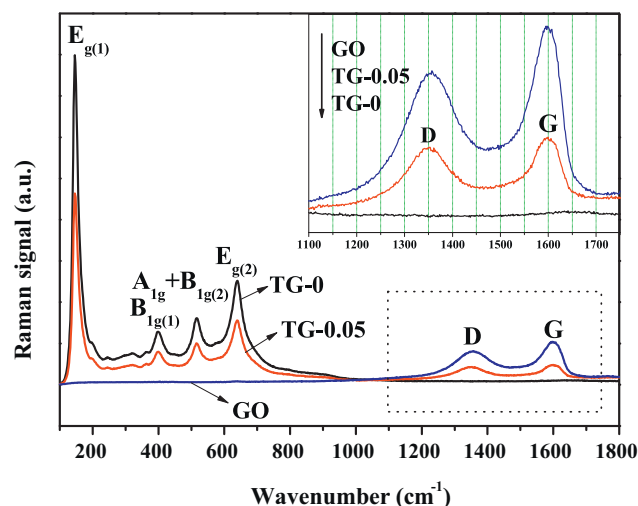


Fig. 2. Raman spectra of the GO, TG-0 and TG-0.05 samples.

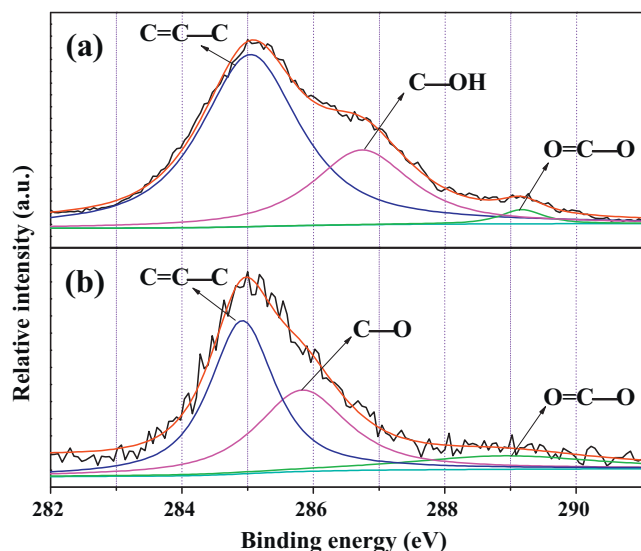


Fig. 3. High-resolution XPS spectra of C 1s for GO (a) and the TG-0.05 (b) sample.

high-resolution C 1s XPS spectra of GO and TiO₂-graphene composite (sample TG-0.05). The C 1s spectrum of GO in Fig. 3a can be fitted into three peaks at 285.0, 286.6 and 289.2 eV, respectively. Two main peaks located at 285.0 and 286.6 eV are usually assigned to adventitious carbon and graphitic carbon from GO, and hydroxyl carbon (C-OH), respectively [34,38,46]. Another small peak located at 289.2 eV can be assigned to carboxyl carbon (O=C-O) [38]. The existence of oxygen-containing carbon in GO can provide active sites for direct connection with TiO₂ particles. In comparison to the GO spectrum, the peak for O=C-O in the TiO₂-graphene composite (Fig. 3b and Table 2) decreases remarkably or almost vanishes, and the peak for C-OH still exists but its intensity is much smaller. This implies that graphene oxide was reduced and the oxygen-containing functional groups were removed during hydrothermal process. Furthermore, the positions of O=C-O and C-OH peaks have obvious shift from 289.2 to 289.0 and 286.6 to 285.8 eV respectively. This suggests that the -OH groups on the surface of TiO₂ particles possibly react with the -COOH and -OH groups on the GO surface through esterification and dehydration to form O=C-O-Ti and C-O-Ti bonds, respectively [38].

3.4. BET surface areas and pore size distributions

Nitrogen adsorption-desorption method is used to investigate the porous structures and BET surface areas of the hierarchical macro/mesoporous TiO₂-graphene composites and pure TiO₂. Fig. 4 shows the nitrogen adsorption-desorption isotherms and the corresponding pore size distribution curves of the TG-0 and TG-0.05 sample. The nitrogen adsorption isotherms for the two samples are similar. The isotherms are of type IV according to BDDT (Brunauer, Deming, Deming and Teller) classification, and have one hysteresis loop at relative pressure between 0.6 and 0.9, indicating pore-size distributions in the mesoporous region [40,41]. These

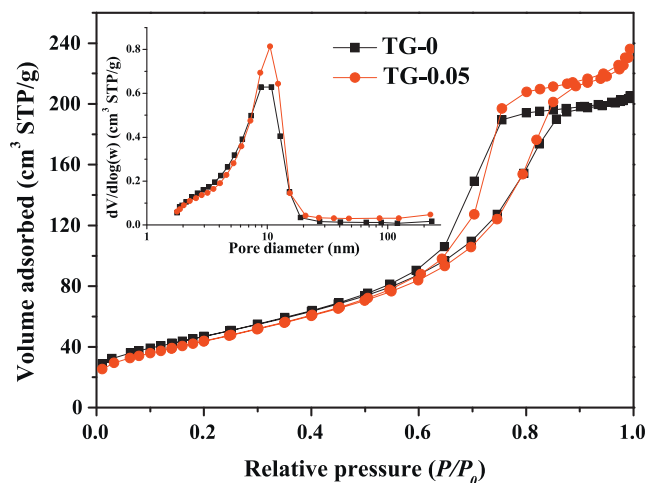


Fig. 4. Nitrogen adsorption-desorption isotherms and the corresponding pore-size distribution curves (inset) of the TG-0 and TG-0.05 samples.

isotherms exhibit H2 hysteresis loops associated with the presence of ink-bottle pores [41]. The corresponding pore-size distributions of the TG-0 and TG-0.05 samples (inset in Fig. 4) are narrow in the range of 2–20 nm, with a peak pore diameter of ca. 10 nm. Table 1 shows that the BET specific surface areas of TiO₂-graphene composites decrease with increasing graphene content. This is due to the fact that the graphene coating on the surface of TiO₂ powders has blocked some mesopores and micropores, resulting in the slight decrease of surface areas and increase of average pore size.

3.5. SEM and TEM analyses

Since N₂ adsorption-desorption analysis could not provide macroporous information of the as-prepared samples, the macroporous structures were observed directly by SEM. Fig. 5 shows SEM images of hierarchical macro/mesoporous TiO₂-graphene powders with different graphene content. When the TBOT was added dropwise to the ethanol-water mixed solution, the contact between the TBOT droplets and distilled water immediately produced a thin, dense semipermeable titania membrane at the droplet interface [40]. Finally, a large white sphere-like particle with size of ca. 3–5 mm was formed. Fig. 5a and b displays the cross-sections of the particle from different directions, while Fig. 5c and d is the surface morphologies of the particle with different magnification. The SEM results indicate that all the prepared TiO₂ samples with or without graphene exhibit disordered macroporous frameworks with continuous walls within the particles, consisting of closely packed aggregates of nanocrystalline titania particles (Fig. 5a and b). The size of 3-dimensional continuous macropores and wall thickness are ca. 1–3 and 1–1.5 μm, respectively. These three-dimensional continuous macroporous channels may serve as ideal light-transport routes for introducing photoenergy and gas molecules into the core space of titania. Further observation indicates that the surface morphologies of TiO₂-graphene powders with different graphene content differ from each other. It can be seen from Fig. 5c that pure TiO₂ (TG-0) has a fold surface with small sphere-like particles deposited on it. The high-magnification SEM image (Fig. 5d) indicates that the surface of the TG-0 sample is relatively smooth with uniform color. However, as for the TG-0.05 sample, except for the same fold surface observed as that of TG-0 (Fig. 5e), some large graphene sheets were observed, which were partially wrapped on the surface of TiO₂ powders, resembling a crumpled silk veil waves (Fig. 5f). With increasing graphene content to 0.2 wt.%, the surface of TiO₂ sample (TG-0.2) was completely covered by graphene sheets, as shown in Fig. 5g and h. The high

Table 2
Results of curve-fitting of high-resolution XPS spectra for the C 1s region of graphene oxide and TiO₂-graphene samples.

Samples		C 1s (C=C-C)	C 1s (C-OH)	C 1s (O=C-O)
GO	<i>E_b</i> (eV)	285.0	286.6	289.2
	<i>r_i</i> (%)	64.6	32.2	3.2
TG-0.05	<i>E_b</i> (eV)	284.9	285.8	289.0
	<i>r_i</i> (%)	72.5	25.7	1.8

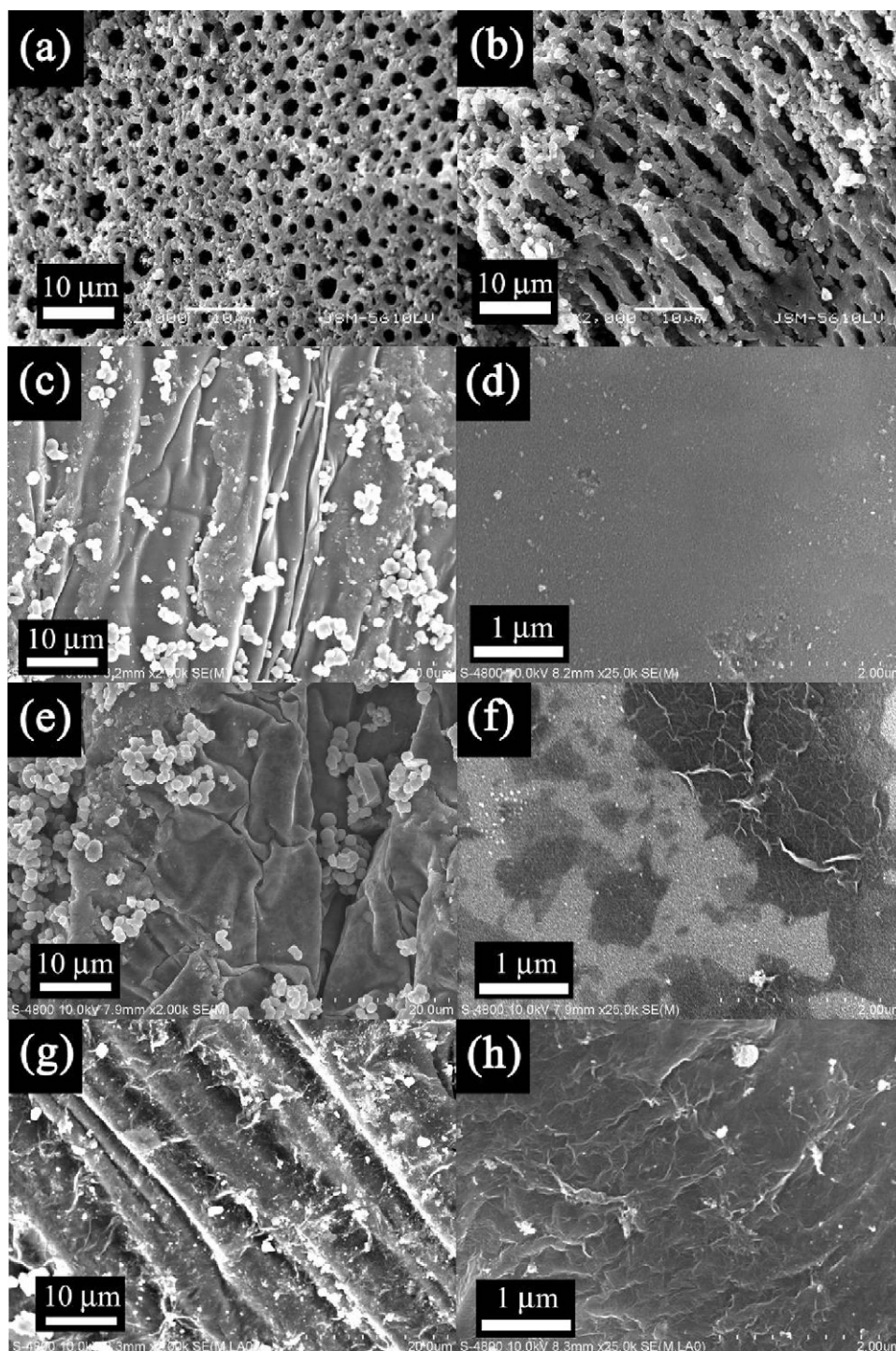


Fig. 5. SEM images of the TiO_2 -graphene composites with different graphene content: TG-0 (a–d), TG-0.05 (e and f) and TG-0.2 (g and h).

coverage would shield TiO_2 from absorbing UV light, resulting in a rapid decrease of irradiation.

The microstructure of TiO_2 -graphene composite was further studied by TEM and HRTEM. Fig. 6a shows the typical TEM image of the TG-0.05 sample. As can be observed from Fig. 6a, the reduced graphene was retained in the form of two-dimensional sheets with micrometre-long wrinkles after the hydrothermal treatment of GO. The TiO_2 nanocrystallites with an average size of ca. 7–8 nm were well dispersed on the graphene sheets due to the interaction between the hydrophilic functional groups (e.g., $-\text{OH}$, $-\text{COOH}$) on GO and the hydroxyl groups on TiO_2 . This intimate interaction

enables the electron to more easily transfer from TiO_2 nanoparticles to graphene sheets during the photoexcitation process. The corresponding HRTEM image (Fig. 6b) shows clear lattice fringes, which allows for the identification of crystallographic spacing. The fringe spacing of ca. 0.35 nm matches that of the (1 0 1) crystallographic plane of anatase TiO_2 [3].

3.6. Photocatalytic activity and mechanism

The photocatalytic activities of the pure TiO_2 and TiO_2 -graphene composite samples were evaluated by photocatalytic degradation

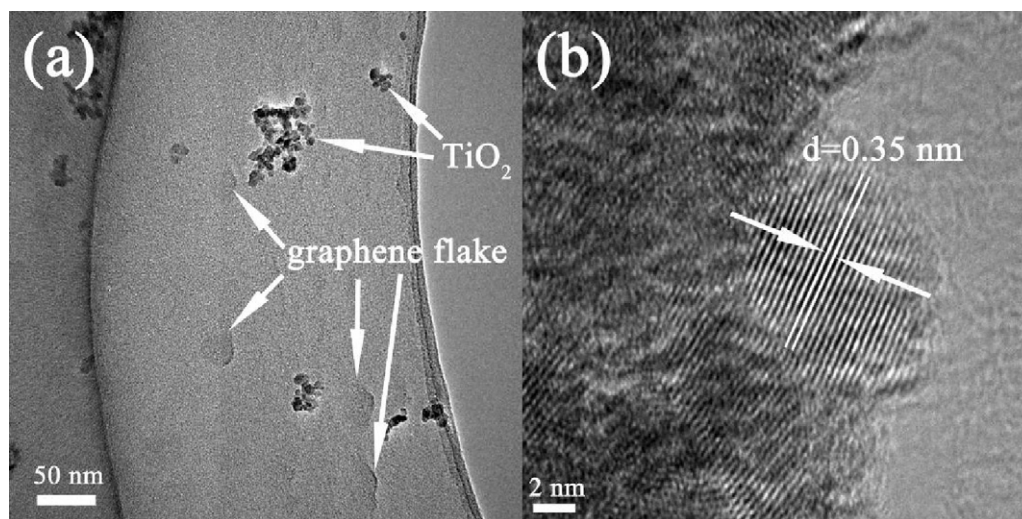


Fig. 6. TEM (a) and HRTEM (b) images of the TG-0.05 sample.

of acetone in air. Fig. 7a displays the comparison of photocatalytic activities (or apparent reaction rate constants) of the TiO₂–graphene samples (TG-0, TG-0.05, TG-0.1 and TG-0.2) and P25. It can be seen that the graphene content has a great effect

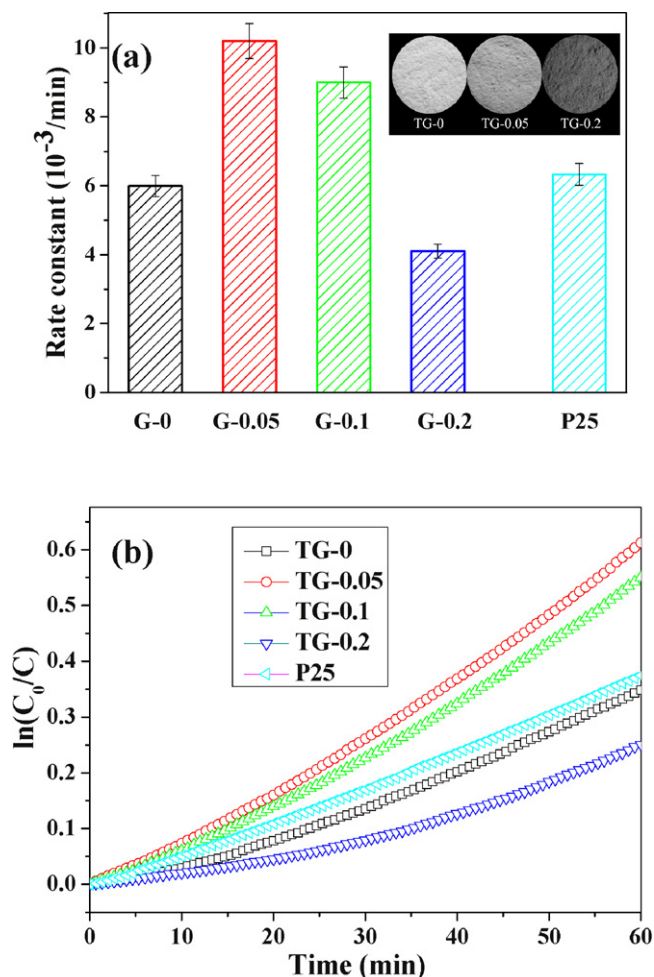


Fig. 7. (a) Comparison of the photocatalytic activity of the TG-0, TG-0.05, TG-0.1, TG-0.2 and P25 samples for the photocatalytic degradation of acetone in air. (b) $\ln(C_0/C)$ as a function of UV irradiation time in the presence of the TiO₂–graphene photocatalysts prepared with different graphene content and P25.

on the photocatalytic activity of TiO₂. The naked TiO₂ sample (TG-0) shows a good photocatalytic activity with a rate constant $k = 5.99 \times 10^{-3}$. This is attributed to the synergetic effects of anatase phase structure, high specific surface area, good crystallinity and hierarchical macro-mesoporous structure. Usually, for anatase TiO₂, a large surface area can offer more active adsorption sites and photocatalytic reaction centers. The hierarchical macro/mesoporous structure is beneficial for enhancing the adsorption efficiency of light and the flow rate of the gas molecules [41]. After introducing only a small amount of graphene, the activity of the sample TG-0.05 is remarkably enhanced and its k value reaches 10.2×10^{-3} , exceeding that of TG-0 and P25 by a factor of 1.7 and 1.6, respectively. A further increase in graphene content higher than 0.05 wt.% leads to decrease of the photocatalytic activity. Especially, at 0.2 wt.% graphene content the photocatalytic activity of the TG-0.2 sample shows a drastic decrease and the k value is even lower than that of TG-0. This is due to the increase in the opacity of TG-0.2 sample (see inset of Fig. 7a) and an excess graphene loading would prevent the light from reaching the surface of the TiO₂. Fig. 7b further shows the kinetics of photocatalytic degradation of acetone in the presence of TiO₂–graphene photocatalysts with different graphene content and P25. Furthermore, the stability of TiO₂–graphene photocatalyst was tested. After three recycles for the photodegradation of acetone, the TiO₂–graphene composites did not exhibit significant loss of activity.

In general, the photocatalytic performance of a photocatalyst is governed by many factors such as surface area, adsorption capacity, light-response range and the recombination rate of photogenerated charge carriers, etc. Herein, we discuss the dominant role of graphene in enhancing the photocatalytic activity of the TiO₂–graphene composites.

Firstly, BET measurements show that the loading of graphene has no significant effect on surface areas of TiO₂–graphene composites due to the low content of graphene (0–0.2 wt.%). The decrease in specific surface area for TiO₂–graphene composites is extremely limited ($<17 \text{ m}^2 \text{ g}^{-1}$, Table 1) and the contribution from graphene to the specific surface area is negligible. In this regard, the variation in adsorption capacity (determined dominantly by the surface area) is not critical for the photoactivity enhancement of TiO₂–graphene composites. Secondly, it has been reported that the high quality of the sp^2 conjugated bond in the carbon lattice of graphene facilitates the electrons to move ballistically in a graphene layer without scattering with mobilities exceeding $15000 \text{ m}^2/(\text{Vs})$ at ambient temperature, which makes graphene perform as an excellent

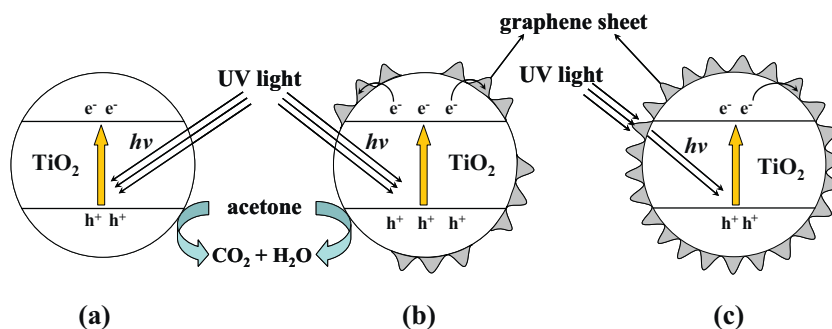
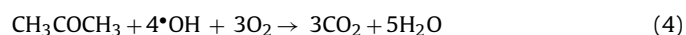
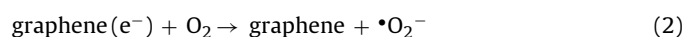


Fig. 8. Schematic illustration for the charge transfer and separation in the TiO₂-graphene composites under UV light irradiation.

electron acceptor [47]. In the present system, the conduction band position of anatase TiO₂ is -0.24 V (vs. SHE), while the potential of graphene/graphene^{•−} is -0.08 V (vs. SHE) [38]. Thus, the photoinduced electrons can be smoothly transferred from the conduction band of TiO₂ to graphene sheets under UV irradiation. A schematic illustration about the mechanism of enhanced photoactivity of the TiO₂-graphene composites is shown in Fig. 8. When the as-prepared samples are irradiated by UV-light, the valence electrons (e[−]) of anatase are excited to the conduction band (CB), creating holes (h⁺) in the valence band (VB). Normally, these charge carriers quickly recombine and only a fraction of electrons and holes participate in photocatalytic reaction, as shown in Fig. 8a. However, when an optimal amount of graphene was incorporated into the TiO₂, the photoinduced electrons on the CB of TiO₂ can further transferred to graphene sheets under UV light irradiation, which effectively retards the recombination of photoinduced electrons and holes (Fig. 8b). These separated electrons and holes are then trapped by some surface adsorbates to generate highly reactive radical species. For example, the holes left in TiO₂ VB can react with adsorbed water molecules (or surface hydroxyl) to form hydroxyl radicals (•OH), and the electrons stored in graphene are trapped by O₂ to form reactive superoxide radical ion (•O₂[−]). Both radical groups (•O₂[−] and •OH) are highly reactive toward acetone degradation. Consequently, high photodegradation activity is achieved over TiO₂ samples as a result of graphene modification. The major reaction steps in this mechanism under UV-light irradiation are summarized in the following equations [48,49]:



However, a higher graphene loading results in the decrease in photocatalytic activity due to the increase in the opacity of TiO₂-graphene samples (Fig. 8c) and a rapid decrease of irradiation passing through the samples.

To further confirm the above suggested photocatalysis mechanism, the transient photocurrent responses were recorded for photoelectrodes consisting of pure TiO₂ (TG-0) and TiO₂-graphene composites (TG-0.05, TG-0.1 and TG-0.2). Fig. 9 shows the *I*-*t* curves for the samples with several on-off cycles of intermittent UV-irradiation. The photocurrent value of TG-0 rapidly decreases to zero when the UV-light irradiation is switched off, and the photocurrent comes back to a constant value when the light is on again, exhibiting a good reproducibility. However, in the case of graphene-modified TiO₂, the photocurrent value gradually increases to a constant value when the light is switched on, and the photocurrent gradually decreases to zero when the light is off. Why do the shapes of photocurrent curves of TiO₂ and graphene-modified TiO₂

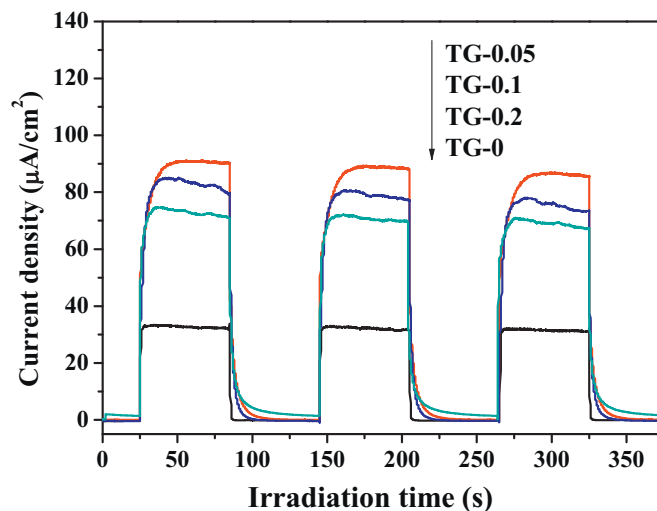


Fig. 9. The transient photocurrent responses of the TG-0, TG-0.05, TG-0.1 and TG-0.2 samples in 1 M Na₂SO₄ aqueous solution under UV light irradiation at 0.5 V vs. Ag/AgCl.

have a great difference? This is due to the fact that when TiO₂ was modified by graphene sheets, the photogenerated electrons on the conduction band of TiO₂ tend to transfer to graphene sheets [38,50]. Thus, the photocurrent was generated by stored electrons from graphene sheets rather than electrons transferred from the conduction band of TiO₂ directly, resulting in the gradually increase in photocurrent. On the other hand, when the light is switched off, due to the electron storage effect of graphene, electrons were gradually released from graphene sheets and further transferred to working electrode, leading to the gradual decrease of photocurrent to zero. The photocurrent response for TiO₂-graphene composites was also reproducible during repeated on/off cycles of illumination. Photocurrent density of ca. 30 μA/cm² was obtained on the pure TiO₂ thin films (TG-0). Surprisingly, a significant increase in photocurrent density (90.7 μA/cm²) was observed when 0.05 wt.% of graphene was incorporated into the TiO₂ (TG-0.05). The observed enhancement in the photocurrent represents improved charge transportation from TiO₂ to graphene to the working electrode surface. Although further increasing the loading of graphene into TiO₂ results in the gradual decrease of the photocurrent, existence of graphene in all composites still results in the enhancement of the photocurrent in comparison to pure TiO₂.

4. Conclusions

In summary, hierarchical macro/mesoporous TiO₂-graphene composites with low loadings (0–0.2 wt.%) of graphene were successfully prepared by a simple hydrothermal and in situ reduction

method. Raman spectra and XPS analysis of TiO₂–graphene composites indicated the reduction of graphene oxide and formation of graphene. The prepared TiO₂–graphene samples showed enhanced photocatalytic activity in photodegradation of acetone in air and graphene content exhibits a great influence on photocatalytic activity. At graphene content = 0.05 wt.%, the TiO₂–graphene composites exhibited the highest photocatalytic activity, which exceeds that of pure TiO₂ and P25 by a factor of 1.7 and 1.6, respectively. The enhanced photocatalytic activity is because graphene can act as an excellent electron acceptor and transporter, thus reducing the recombination of charge carriers and enhancing the photocatalytic activity. The transient photocurrent response experiment further confirmed the transfer of photogenerated electrons from conduction band of TiO₂ to graphene. The prepared hierarchical macro/mesoporous structured TiO₂–graphene composites should also find widely potential applications in photocatalysis, catalysis, solar-cell, separation, and purification processes.

Acknowledgments

This work was partially supported by National Basic Research Program of China (2009CB939704), National Natural Science Foundation of China (20877061 and 51072154), Natural Science Foundation of Hubei Province (2010CDA078) and Self-determined and Innovative Research Funds of SKLWUT.

References

- [1] M.A. Fox, M.T. Dulay, *Chem. Rev.* 93 (1993) 341.
- [2] M.R. Hoffmann, S.T. Martin, W. Choi, D.W. Bahnemann, *Chem. Rev.* 95 (1995) 69.
- [3] J.G. Yu, W.G. Wang, B. Cheng, B.L. Su, *J. Phys. Chem. C* 113 (2009) 6743.
- [4] J.G. Yu, W.G. Wang, B. Cheng, *Chem. Asian J.* 5 (2010) 2499.
- [5] X.X. Yu, S.W. Liu, J.G. Yu, *Appl. Catal. B: Environ.* 104 (2011) 12.
- [6] Y.W. Cheng, R.C.Y. Chan, P.K. Wong, *Water Res.* 41 (2007) 842.
- [7] Y.X. Li, G.X. Lu, S.B. Li, *J. Photochem. Photobiol. A* 152 (2002) 219.
- [8] O. Carp, C.L. Huisman, A. Reller, *Prog. Solid State Chem.* 32 (2004) 33.
- [9] H. Park, W. Choi, *J. Phys. Chem. B* 108 (2004) 4086.
- [10] J.M. Herrmann, H. Tahiri, Y. Ait-Ichou, G. Lassaletta, A.R. González-Elipe, A. Fernández, *Appl. Catal. B* 13 (1997) 219.
- [11] Q. Li, B.D. Guo, J.G. Yu, J.R. Ran, B.H. Zhang, H.J. Yan, J.R. Gong, *J. Am. Chem. Soc.* 133 (2011) 10878.
- [12] S.W. Liu, J.G. Yu, M. Jaroniec, *J. Am. Chem. Soc.* 132 (2010) 11914.
- [13] Q.J. Xiang, J.G. Yu, M. Jaroniec, *Chem. Soc. Rev.* 41 (2012) 782.
- [14] K. Pomoni, A. Vomvas, C. Trapalis, *Thin Solid Films* 479 (2005) 160.
- [15] M. Ksibi, S. Rossignol, J.M. Tatibouet, C. Trapalis, *Mater. Lett.* 62 (2008) 4204.
- [16] S.G. Kumar, L.G. Devi, *J. Phys. Chem. A* 115 (2011) 13211.
- [17] L.G. Devi, N. Kottam, S.G. Kumar, *J. Phys. Chem. C* 113 (2009) 15593.
- [18] C.Z. Wen, H.B. Jiang, S.Z. Qiao, H.G. Yang, G.Q. Lu, *J. Mater. Chem.* 21 (2011) 7052.
- [19] Q.J. Xiang, J.G. Yu, W.G. Wang, M. Jaroniec, *Chem. Commun.* 47 (2011) 6906.
- [20] J.G. Yu, Q.J. Xiang, M.H. Zhou, *Appl. Catal. B: Environ.* 90 (2009) 595.
- [21] S. Sakthivel, M.V. Shankar, M. Palanichamy, B. Arabindoo, D.W. Bahnemann, V. Murugesan, *Water Res.* 38 (2004) 3001.
- [22] J.G. Yu, Q.L. Li, Z. Shu, *Electrochim. Acta* 56 (2011) 6293.
- [23] J.G. Yu, T.T. Ma, S.W. Liu, *Phys. Chem. Chem. Phys.* 13 (2011) 3491.
- [24] J.G. Yu, T.T. Ma, G. Liu, B. Cheng, *Dalton Trans.* 40 (2011) 6635.
- [25] Y. Yao, G.H. Li, S. Ciston, R.M. Lueptow, K.A. Gray, *Environ. Sci. Technol.* 42 (2008) 4952.
- [26] Y.Z. Long, Y. Lu, Y. Huang, Y.C. Peng, Y.J. Lu, S.Z. Kang, J. Mu, *J. Phys. Chem. C* 113 (2009) 13899.
- [27] W.D. Wang, C.G. Silva, J.L. Faria, *Appl. Catal. B: Environ.* 70 (2007) 470.
- [28] K.S. Novoselov, A.K. Geim, S.V. Morozov, D. Jiang, Y. Zhang, S.V. Dubonos, I.V. Grigorieva, A.A. Firsov, *Science* 306 (2004) 666.
- [29] M.J. Allen, V.C. Tung, R.B. Kaner, *Chem. Rev.* 110 (2010) 132.
- [30] Y.Q. Sun, Q.O. Wu, G.Q. Shi, *Energy Environ. Sci.* 4 (2011) 1113.
- [31] D.H. Wang, D.W. Choi, J. Li, Z.G. Yang, Z.M. Nie, R.D. Kou, H. Hu, C.M. Wang, L.V. Saraf, J.G. Zhang, I.A. Aksay, J. Liu, *ACS Nano* 3 (2009) 907.
- [32] A.N. Cao, Z.S. Liu, S. Chu, M.H. Wu, Z.M. Ye, Z.W. Cai, Y.L. Chang, S.F. Wang, Q.H. Gong, Y.F. Liu, *Adv. Mater.* 22 (2010) 103.
- [33] Y.H. Ng, A. Iwase, A. Kudo, R. Amal, *J. Phys. Chem. Lett.* 1 (2010) 2607.
- [34] E. Gao, W.Z. Wang, M. Shang, J.H. Xu, *Phys. Chem. Chem. Phys.* 13 (2011) 2887.
- [35] L. Jia, D.H. Wang, Y.X. Huang, A.W. Xu, H.Q. Yu, *J. Phys. Chem. C* 115 (2011) 11466.
- [36] Q.J. Xiang, J.G. Yu, M. Jaroniec, *J. Phys. Chem. C* 115 (2011) 7355.
- [37] H. Zhang, X.J. Lv, Y.M. Li, Y. Wang, J.H. Li, *ACS Nano* 4 (2009) 380.
- [38] Q.J. Xiang, J.G. Yu, M. Jaroniec, *Nanoscale* 3 (2011) 3670.
- [39] J. Du, X.Y. Lai, N.L. Yang, J. Zhai, D. Kisailus, F. Su, D. Wang, L. Jiang, *ACS Nano* 5 (2010) 590.
- [40] J.G. Yu, Y.R. Su, B. Cheng, *Adv. Funct. Mater.* 17 (2007) 1984.
- [41] J.G. Yu, L.J. Zhang, B. Cheng, Y.R. Su, *J. Phys. Chem. C* 111 (2007) 10582.
- [42] S.W. Liu, J.G. Yu, M. Jaroniec, *Chem. Mater.* 23 (2011) 4085.
- [43] J.G. Yu, Y.R. Su, B. Cheng, M.H. Zhou, *J. Mol. Catal. A* 258 (2006) 104.
- [44] J.G. Yu, W.G. Wang, B. Cheng, B.B. Huang, X.Y. Zhang, *Res. Chem. Intermed.* 35 (2009) 653.
- [45] D.R. Dreyer, S. Murali, Y.W. Zhu, R.S. Ruoff, C.W. Bielawski, *J. Mater. Chem.* 21 (2011) 3443.
- [46] O. Akhavan, E. Ghaderi, *J. Phys. Chem. C* 113 (2009) 20214.
- [47] G.X. Wang, J. Yang, J. Park, X.L. Gou, B. Wang, H. Liu, J. Yao, *J. Phys. Chem. C* 112 (2008) 8192.
- [48] W. Choi, J.Y. Ko, H. Park, J.S. Chung, *Appl. Catal. B: Environ.* 31 (2001) 209.
- [49] J. Yu, S. Liu, H. Yu, *J. Catal.* 249 (2007) 59.
- [50] Y.H. Ng, I.V. Lightcap, K. Goodwin, M. Matsumura, P.V. Kamat, *J. Phys. Chem. Lett.* 1 (2010) 2222.